Geophysical Journal International

Geophys. J. Int. (2016) **205,** 1574–1588
Advance Access publication 2016 March 14
GJI Geodynamics and tectonics

doi: 10.1093/gji/ggw104

Dynamics and excess temperature of a plume throughout its life cycle

N. Cagney and C. Lithgow-Bertelloni

Department of Earth Sciences, University College London, Gower Street, London, WC1E 6BT, *United Kingdom. E-mail: neil.cagney.11@ucl.ac.uk*

Accepted 2016 March 10. Received 2016 March 9; in original form 2015 December 14

SUMMARY

Measurements of the velocity field associated with plumes rising through a viscous fluid are performed using stereoscopic Particle-Image Velocimetry in the Rayleigh number range 4.4 $\times$ 10^5–6.4 $\times$ 10^5. The experimental model is analogous to a mantle plume rising from the core–mantle boundary to the base of the lithosphere. The behaviour of the plume is studied throughout its life cycle, which is broken up into four stages; the Formation Stage, when the plume forms; the Rising Stage, when the plume rises through the fluid; the Spreading Stage, when the plume reaches the surface and spreads; and finally the Declining Stage, when the heat source has been removed and the plume weakens. The latter three stages are examined in terms of the Finite-Time Lyapunov Exponent fields and the advection of passive tracers throughout the flow. The temperature at the heater and near the fluid surface are measured using thermocouples to infer how the presence of a mantle plume would produce excess temperature near the lithosphere throughout the various stages of its life cycle. In all experiments, a time lag is observed between the removal of the heat source and the decline in the excess temperature near the surface, which is proportional to the rise time. A simple analytical model is presented, which suggests that under mantle conditions (i.e. negligible thermal diffusion), the relationship between the time lag and the rise time is robust and independent of the Rayleigh number; however, the constant of proportionality is closer to unity in the absence of diffusion. Once the heat source is removed, the excess temperature near the surface declines exponentially at a rate that is inversely proportional to the rise time. The implications of this result are discussed in terms of the decline in volcanism in the Louisville hotspot chain over the past 20 Ma. The rise velocity of material in the plume is examined; the rise velocity is found to vary significantly with the plume height in a manner that is inconsistent with many of the common semi-analytical models of thermal plumes in the literature. It is also argued that this height dependency will cause estimates of the rise velocity based on the decay series of uranium isotopes to significantly underestimate the true value.

Key words: Heat flow; Mantle processes; Dynamics: convection currents, and mantle plumes; Heat generation and transport; Hotspots.

1 INTRODUCTION

Mantle plumes are columns of hot material that rise from a thermal boundary in the mantle and are thought to be a cause of intraplate volcanism (Morgan 1971; Richards *et al.* 1989). The behaviour of plumes is important in terms of understanding the heat flow within the Earth's interior (Lay *et al.* 2008) and can provide insight into the mixing history and chemical composition of the mantle (Kellogg 1992). The geochemical signature of Ocean Island Basalts (OIBs), which are generally attributed to the presence of a mantle plume, is distinct from that of Mid-Ocean Ridge Basalts (MORBs) which are derived from the depleted upper mantle (Hofmann 1997; Hart *et al.* 1992). In order to fully understand the origin of the geochemical signature of OIBs and ultimately to use this data to gain insight into the chemical composition of the mantle, it is first necessary to understand the behaviour of a thermal plume as it passes through a fluid and reaches the surface.

The behaviour of a thermal plume and the nature of heat flow in the mantle are controlled by the Rayleigh number,

$$Ra = \frac{\rho \alpha \Delta T g D^3}{\mu \kappa} \tag{1}$$

where ρ is the density, α is the coefficient of thermal expansion, g is the acceleration due to gravity, ΔT is the temperature difference across the domain, D is the depth of the domain, and μ and κ are the dynamic viscosity and thermal diffusivity, respectively. The Rayleigh number in the mantle is thought to be of the order of $\sim 10^7$,

implying that it convects vigorously over geological timescales and is likely to contain several plumes.

There have been some recent quantitative experimental measurements of the velocity and temperature fields associated with thermal plumes (Davaille & Vatteville 2005; Kumagai *et al.* 2007; Davaille *et al.* 2011; Cagney *et al.* 2015). However, the majority of studies have been qualitative in nature, typically either using dyes to visualize the flow (e.g. Olson & Singer 1985; Griffiths & Campbell 1990, 1991; Bercovici & Mahoney 1994) or shadowgraphs to image the temperature field (e.g. Schlien 1976; Moses *et al.* 1993). In flow visualization studies, it is common to inject buoyant dyed material into an ambient fluid rather than providing a direct heat source, even though this is likely to have a significant effect on the dynamics (Farnetani & Richards 1995). This may be a contributing factor to the inconsistencies between various scaling laws regarding thermal plumes in the literature (e.g. Batchelor 1954; Griffiths & Campbell 1990; Moses *et al.* 1993; Bercovici & Mahoney 1994).

A general feature in all these studies is that when the buoyant fluid is less viscous than the ambient material, the plume has a large bulbous head followed by a narrow stem. The formation of Large Igneous Provinces (LIPs) is generally thought to be associated with the arrival of the head at the lithosphere, while volcanic chains are attributed to the interaction between the stem and the overriding plate (Richards *et al.* 1989; Campbell & Griffiths 1990).

Despite the crucial role that plume-lithosphere interaction is likely to play in the formation of LIPs and OIBs, very few experimental studies have examined the dynamics and temperature effects associated with the arrival of a thermal plume at the surface (although the problem has been approached numerically (Parmentier & Turcotte 1975; Ribe & Christensen 1994; Farnetani & Richards 1995; Farnetani & Hofmann 2010; Ballmer *et al.* 2011). Kerr & Mériaux (2004) and Richards & Griffiths (1988) used flow visualization to study the effects of a moving plate at the surface on the plume dynamics, but their studies did not include temperature measurements.

Another aspect of the behaviour of plumes that has received little attention to date is the final stage of their life cycle, when their local source of heat becomes depleted, the buoyancy flux declines and the hotspot eventually become extinct. One example of such an extinct hotspot is the McKenzie LIP in Canada (LeCheminant & Heaman 1989). Similarly, volcanic activity in the Louisville hotspot track is known to have declined in the past 20 Ma (Lonsdale 1988), although it is not clear whether the underlying plume is becoming extinct, or whether it is simply a fluctuation in buoyancy flux, as occurs in other hotspots (Parnell-Turner *et al.* 2014). The tomographic studies of Montelli *et al.* (2004, 2006) revealed a 'catalogue' of plumes throughout the mantle, many of which did not appear to originate from a thermal boundary, suggesting that the local heat source of these plumes had become depleted and the plumes were becoming extinct. While it may be argued that some of these plume features are attributable to the difficulty in resolving plumes at depth (e.g. French & Romanowicz 2015), it raises the question as to how a plume in the final stage of its life cycle would appear in a seismic study, and how this decline in buoyancy flux would affect the fluid dynamics of the plume and its heating effect on the lithosphere.

This paper has two main objectives; first, to gain a deeper understanding of the dynamics and heat transfer associated with the ideal case of an isolated thermal plume, and second, to investigate to what extent these findings may be applied to conditions in the mantle. We present quantitative measurements of the velocity field associated with a thermal plume and simultaneous temperature measurements near the fluid surface. The experimental model is interpreted as analogous to a mantle plume rising from the core-mantle boundary (CMB) to the lithosphere (although the data can equally be interpreted as a plume rising from the 660 km discontinuity). Given the uncertainty in the variations in material properties between the upper and lower mantle and the effects of partial melting on the mantle properties (as well as the difficulties in experimentally modelling these effects accurately) we have chosen to neglect the effects of phase transitions and decompression melting. No shear force is applied to the surface of the fluid, and therefore in the analogous case in the mantle the lithospheric plate must have a low velocity relative to the plume motion, e.g. the slow-moving African plate.

The remainder of the paper is structured as follows; Section 2 describes the experimental system and post-processing algorithms used to perform the measurements; the dynamics and surface temperature associated with a single high Ra experiment at different stages in the plume's life cycle are presented in Sections 3.1–3.4; the variation in the rise velocity of the plume with depth and time are discussed in Section 3.5; the effect of the Rayleigh number on the dynamics are explored in Section 4; Section 6 discusses the relevant timescales of the plume dynamics and the implications for the mantle; and finally some concluding remarks are made in Section 7.

2 EXPERIMENTAL DETAILS

The experiments were performed in a cubic test-section, which had 10 mm thick Perspex walls and internal dimensions (i.e. the width of the fluid domain) of 265 mm, as shown in Fig. 1. A circular heater with a diameter of 20 mm was installed in the centre of the tank, flush with the bottom surface. The heater was made of copper, and was embedded with an electrical heating element and a thermocouple to monitor the temperature. The origin of the reference frame is taken as the centre of the heater, with x and y measured in the horizontal and vertical directions, respectively. In the experiments described in this paper, the heater temperature was set to $T_{\max} = 53$–$67.7\,^{\circ}\mathrm{C}$ (Table 1), within $\pm 0.5\,^{\circ}\mathrm{C}$. The ambient temperature measured at the heater was $T_{\mathrm{amb}} = 20.8\,^{\circ}\mathrm{C}$, which gave an applied temperature difference of $\Delta T = 32.2$–$46.9\,^{\circ}\mathrm{C}$. The latter case represents the maximum temperature of the heater.

The time at which the heater was turned on is defined as $t = 0$. It reached the target temperature within 10–15 min and it was turned off at t_{co} (referred to as the 'cut-off time'), long after the plume had reached the fluid surface.

The tank was filled with corn syrup (LSI Speciality Products' Liquidose 436) to a depth of 254.2 mm. A thermocouple was inserted into the syrup directly above the heater, 8.9 mm below the fluid surface. The temperature signals from this thermocouple and the one in the heater were recorded at a sampling frequency of 2 Hz for a period of 10 hr. The temperature recording started several minutes before the heater was turned on in order to measure the ambient temperature.

The temperature signal measured at the heater, T_h, was non-dimensionalized as

$$\Theta_H(t) = \frac{T_h(t) - T_{h,\mathrm{amb}}}{T_{\max} - T_{h,\mathrm{amb}}}, \tag{2}$$

where $T_{h,\mathrm{amb}}$ is the ambient temperature at the heater before it was turned on. The temperature signal recorded near the surface, $T_s(t)$ was non-dimensionalized in a similar fashion,

$$\Theta_S(t) = \frac{T_s(t) - T_{s,\mathrm{amb}}}{T_{\max} - T_{s,\mathrm{amb}}}. \tag{3}$$

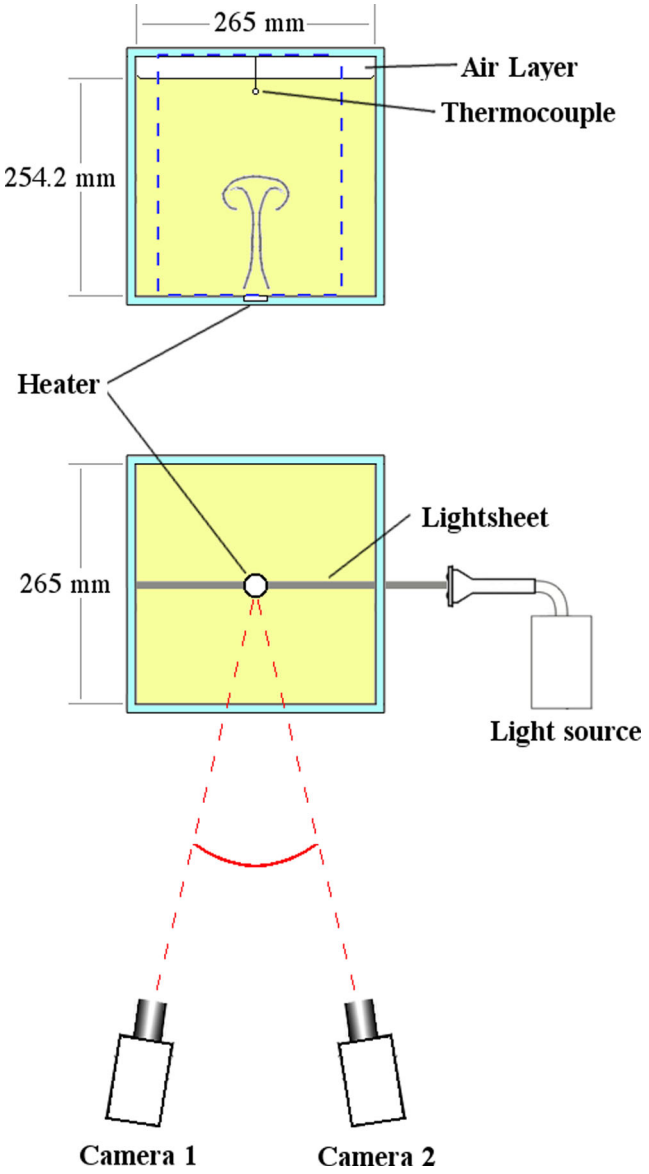

Figure 1. Elevation (top) and plan (bottom) view of the test-section and PIV system. The dashed blue line in the elevation view indicates the boundary of the PIV domain.

There was a small thermal gradient across the test-section, which meant that the ambient temperature at the surface was slightly hotter than the ambient temperature at the heater. Weak lateral temperature gradients also meant that at lower ΔT values plumes rising through the test section were deflected slightly from the central axis where the thermocouple was positioned, causing anomalously low Θ_S values and making the signals un-useable. Therefore no results are presented for $\Delta T < 30\,^{\circ}\mathrm{C}$.

The dynamic viscosity of the syrup was measured using a viscometer (Viscometer 7 Plus, Haake) over the temperature range 24.4–69.5 °C (which approximately spanned the temperature range of the experiments) and was found to vary as

$$\mu = 327.3\mathrm{e}^{-0.0827T}, \tag{4}$$

where T is the temperature in degrees Celsius. This corresponds to a maximum viscosity contrast of 14.4–48.3 in the three experiments. Hydrometers (Thermo Fisher Scientific) were used to measure the density, which was 1439.4 kg m^{-3} at ambient temperature and the coefficient of thermal expansion was $3.53 \times 10^{-4}\,^{\circ}\mathrm{C}^{-1}$. The thermal diffusivity, as provided by the manufacturer, was $1.04 \times 10^{-7}\mathrm{m}^2\mathrm{s}^{-1}$. Combining these properties at the ambient temperature, the syrup had a kinematic viscosity of $\nu = 0.041$ m^2 s^{-1} and a Prandtl number of $Pr = \nu/\kappa = 3.92 \times 10^5$. The Peclet number, $Pe = \overline{v}_{\mathrm{mid}} D/\kappa$, describes the relative importance of thermal convection and conduction, where $\overline{v}_{\mathrm{mid}}$ is the characteristic velocity, here defined as the mean vertical velocity along the plume axis in the centre of the test-section, over the time span between the plume reaching the surface and the heater being switched off. The values of $\overline{v}_{\mathrm{mid}}$ and the corresponding Peclet numbers for each experiment are listed in Table 1. In each case, Pe is large, indicating that heat transfer occurs primarily by convection.

Table 1. Summary of the experimental parameters used in each experiment. See the text for a description of each variable.

Parameter	Experiment 1	Experiment 2	Experiment 3
$T_{\max}$	53 °C	60.9 °C	67.7 °C
ΔT	32.2 °C	40.1 °C	46.9 °C
Ra	4.4×10^5	5.48×10^5	6.4×10^5
$\mu_{\max}/\mu_{\min}$	14.4	27.6	48.3
Δt	95 s	80 s	65 s
t_{co}	220.4 min	183.2 min	118.7 min
Number of PIV fields	149	151	181
$\overline{v}_{\mathrm{mid}}$	0.103 mm s^{-1}	0.127 mm s^{-1}	0.171 mm s^{-1}
Pe	252.7	310.4	416.9

In practice, the high viscosity of the syrup meant that it was difficult to ensure that no bubbles or air pockets were present at the top of the tank when the test-section was filled. To avoid this problem, which would have made the flow asymmetric, a thin layer of air was left above the syrup across the entire test-section, as shown in Fig. 1. This meant that the fluid domain had a free-slip condition at the upper surface. Griffiths & Campbell (1991) studied the spreading of thermally and chemically buoyant blobs as they reached the surface of a viscous syrup, and found that the behaviour was not significantly affected by the presence of either a free-slip or no-slip condition (i.e. a solid boundary), although the blobs spread out slightly faster in the former case.

Steroscopic Particle-Image Velocimetry (PIV) was used to measure the three-component velocity field in one of the symmetry planes passing through the plume axis, as shown in Fig. 1. A complete description of the technique can be found in Raffel *et al.* (2007). The measurement plane was illuminated using a light-source, optical fibre and line generator (Volpi), and the flow was uniformly seeded with a high-gloss polymer powder, which has a variable diameter in the range 1–40 μm. Two CCD cameras, separated by 18 ° were used to acquire the images. By using two cameras at different angles, the velocity fields could be combined to find the velocity component normal to the measurement plane, which cannot be resolved using non-stereoscopic PIV (Raffel *et al.* 2007; Westerweel *et al.* 2013). A two-pass cross-correlation scheme was used to estimate the velocity fields in each camera. Following each pass, the normalized median test (Westerweel & Scarano 2005) was applied, and erroneous vectors were replaced by the local median. The final vector fields spanned the horizontal region $x = -110.6$ mm to 87.14 mm, and $y = 1.73$ mm to 265.37 mm vertically, which is hereafter referred to as the PIV domain. The domain extends slightly above the upper surface of the fluid, but vectors in this region were simply ignored. The PIV measurements had a spatial resolution of 3.47 mm in both the vertical and horizontal directions. Standard PIV is not effective at measuring the velocity near solid boundaries

(Nguyen *et al.* 2010), and therefore it was not possible to resolve the velocity lower than 1.73 mm above the bottom of the test-section.

The heater was turned on as the second velocity field was acquired ($t = 0$), and the first field (acquired at $t < 0$) was used to ensure that there was no significant background flow (e.g. flow due to small thermal gradients across the test-section). The temperature signals from the thermocouples were recorded for several hours after the last PIV field was acquired.

2.1 Lagrangian measurements

The PIV vectors are computed in an Eulerian reference frame (i.e. one that is fixed in space and does not moved with the flow). However, it can be difficult to identify the characteristics of convecting flow features such as plumes in an Eulerian frame, and it is often beneficial to convert the measurements into a Lagrangian frame (i.e. one which moves with the major flow features) (O'Farrell & Dabiri 2010; Cagney *et al.* 2015).

In order to do this, once the PIV fields have been acquired, they are seeded with passive tracers which can be numerically advected forwards or backwards in time using a Runge–Kutta scheme (Ferziger 1998). Using this approach, it is possible to identify the origin and final destination of the material at any point in the PIV domain at any given time. Of particular interest to this study is the identification of the location from which each region of fluid originated at $t = 0$. This information can be extended to provide an indication from where in the mantle the geochemical signature of OIBs originated, and ultimately to make inferences on the nature of the mantle. At a given time-step, t_i, the PIV domain was seeded with 304 × 228 passive tracers (i.e. the tracer field had three times the spatial resolution of the vector fields), which were advected back in time to $t = 0$. Thus the origin of the material throughout the PIV domain could be calculated at any time. These fields are hereafter referred to as the 'tracer fields' and are presented with the colour indicating the depth from which the material at each point originated.

The Lagrangian Coherent Structures (LCSs) of a system are lines or surfaces that separate qualitatively distinct regions of the flow, and can be useful in terms of revealing underlying patterns in complex flows. The LCSs can be approximated from elevated regions in the Finite-Time Lyapunov Exponent (FTLE) fields, σ_f, which can be calculated from the trajectories of the passive tracers (Shadden *et al.* 2005; Haller 2015). At the start of the tracer advection, t_0, the tracers are uniformly spaced with a separation, $\delta\mathbf{x}(t_0)$. In practice, $\delta\mathbf{x}$ is taken as the largest real eigenvalue of the Cauchy-Green deformation tensor. As the flow progresses, the separation between tracers which were initially neighbouring will increase, at most exponentially. This separation or stretching rate is captured by the FTLE:

$$\sigma_f(\mathbf{x}, t) = \frac{1}{|t - t_0|} \log\left(\frac{\max(||\delta\mathbf{x}(t)||)}{||\delta\mathbf{x}(t_0)||}\right). \quad (5)$$

Regions of high $\sigma_f(\mathbf{x}, t)$ indicate areas where the local tracers separate rapidly with time, indicating strong fluid stretching. The FTLE fields can also be calculated in backwards-time, by reversing the flow and advecting the tracers backwards from t to t_0. In this case, regions of high FTLE correspond to regions that *have already* undergone strong stretching or deformation. The backward-time variant of the FTLE fields, denoted as $\sigma_f^-(\mathbf{x}, t)$, has previously been shown to effectively delineate the boundary between the plume head and the ambient fluid (Cagney *et al.* 2015), and is here used to visualize the plume structure.

Table 2. Summary of fluid properties of corn syrup at ambient temperature, and estimates of the corresponding properties of material in the mantle. The density and viscosity values for the mantle were taken as a weighted average of the estimates of the upper and lower mantles, based on their relative masses (see table 3.1 of Schubert *et al.* 2001). The *Pe* values in the mantle were calculated assuming a plume rise velocity of ∼5 cm a^{-1}.

Property	Experiments	Mantle	Upper Mantle	Units
ρ^a	1439.4	4530	3560	[kg m^{-3}]
α^b	3.53×10^{-4}	3×10^{-5}	3×10^{-5}	[°C^{-1}]
ΔT	32.2–46.9	2150	300	[°C]
D	254.2×10^{-3}	2.8×10^{6}	0.57×10^{6}	[m]
μ^c	57.6	1.5×10^{22}	3.5×10^{20}	[Pa s]
κ^b	0.104×10^{-6}	0.8×10^{-6}	0.8×10^{-6}	[m^2 s^{-1}]
Pr	3.92×10^{5}	4.1×10^{24}	1.2×10^{23}	[–]
Ra	$4.4–6.4 \times 10^{5}$	5.2×10^{6}	2.1×10^{5}	[–]
Pe	>250	∼6000	∼1100	[–]

[a]Schubert *et al.* (2001), table 3.1, p. 69.
[b]Schubert *et al.* (2001), table 11.3, p. 512.
[c]Kaufmann & Lambeck (2000).

The σ_f^- fields at each time step were found by advecting the tracers backwards in time fifty time-steps (which in terms of eq. (5) corresponds to $t_0 = t - 50\Delta t$). For the first fifty time-steps, the tracers were simply advected back to $t_0 = 0$. When tracers were advected outside the PIV domain, the local σ_f^- value was calculated using the time at which the tracer left the domain.

2.2 Rayleigh numbers

Table 2 summarizes the fluid properties of the corn syrup used in the current work and estimates of the corresponding values for the mantle. The values corresponding to the upper mantle are relevant to plumes which may form at the 660 km discontinuity, as described by Courtillot *et al.* (2003). The depth of the fluid domain does not include the rigid lithosphere, which is taken here to have a thickness of 100 km. The temperature difference across the mantle was found by taking the temperature at the CMB to be 3500 °C (Lay *et al.* 2008), and taking the temperature in the lithosphere-asthenosphere boundary to be approximately 1350 °C (Kawakatsu *et al.* 2009). White (2010) summarized various geochemical estimates of the excess temperature associated with mantle plume near the surface, which tend to occur in the range 100–300 °C. The upper limit of this range is taken as an approximation of the temperature difference across the upper mantle for plumes forming at the boundary between the upper and lower mantles.

Many of the values in Table 2 are likely to vary with depth and temperature; however, they give a representative value for the conditions occurring in the mantle and facilitate comparison with the current experimental system. Inserting the various values into eq. (1), the Rayleigh number for a plume rising from the CMB and rises through the entire mantle is 5.2×10^6, while a plume forming in the upper mantle will have Rayleigh number of approximately 2.1×10^5. The Rayleigh number in our experiments ranges between 4.4×10^5 and 6.4×10^5, which is of a very similar magnitude, indicating that the results presented here are also representative of the dynamics of both types of plumes in the mantle.

The Peclet numbers are also presented, assuming a rise velocity of ∼5 cm a^{-1} for plumes in both the upper and lower mantle. This value results an approximate Peclet number of $Pe \sim 10^3$–10^4. This range is approximately 1–2 orders of magnitude greater than that of the experiments, but indicates that in both cases heat transfer occurs primarily by convection rather than conduction.

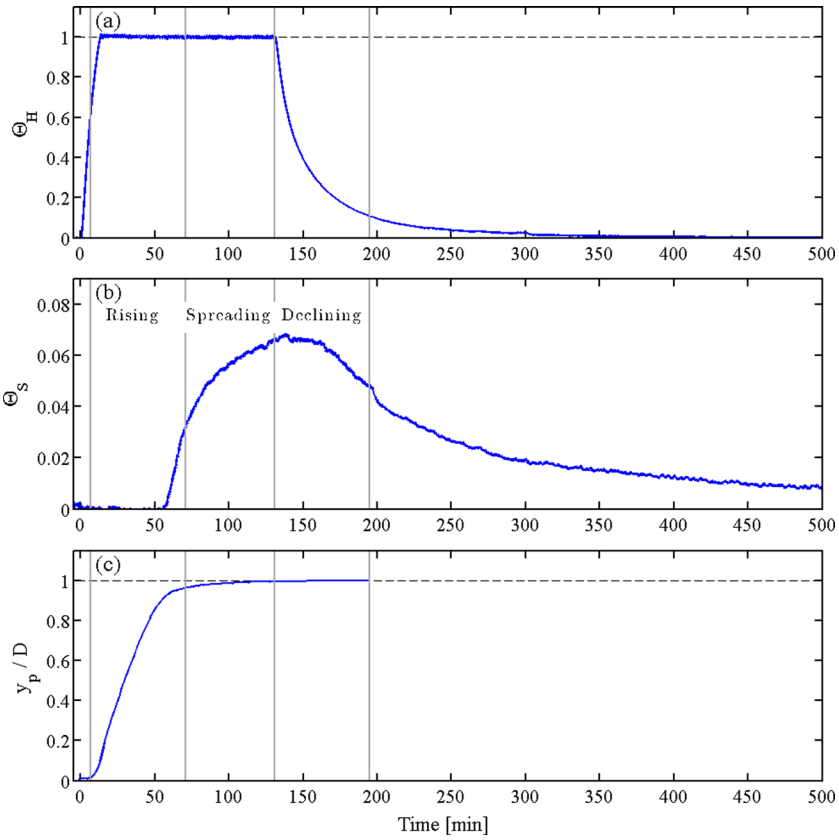

Figure 2. Time-series of the non-dimensional temperature signals measured at the heater (a) and near the surface (b), and the variation in the height of the plume (c). The vertical grey lines mark the boundaries between the different stages of the plume's life cycle, as defined in Table 3.

3 RESULTS

3.1 $Ra = 6.4 \times 10^5$

The dynamics of the plume and its effect on the surface temperature were similar in all experiments. It is therefore useful to examine a single experiment in detail here (the $Ra = 6.4 \times 10^5$ case) in order to demonstrate the key stages of plume's life cycle. Figs 2(a) and (b) show the non-dimensional temperature signals measured at the heater and near the top of the fluid domain, respectively. The heater temperature reaches the target value (i.e. $\Theta_H = 1$) at $t = 13.3$ min, where it remains steady to within ± 0.01 (i.e. $\pm 0.5\,^{\circ}$C), until the heater is turned off and the temperature gradually declines.

The surface temperature in Fig. 2(b) shows a somewhat more irregular trend. The temperature at the surface does not begin to show an increase until approximately $t = 55$ min, reflecting the amount of time taken for the heat at the base of the test-section to rise through the fluid. The heater temperature then continues to increase, reaching a maximum at $t = 138.7$ min, shortly after the heater has been turned off. At around $t = 164$ min the temperature signal at the surface starts to decline and gradually decays.

Fig. 2(c) shows the variation in the non-dimensional height of the plume, $y_p(t)/D$, which was measured as the highest point at $x = 0$ at which the local passive tracers originated from below the PIV domain ($y \leq 1.73$ mm). The plume height remains low until $t \sim 10$ min, shortly before the heater reaches the applied temperature. After this point, the plume rises rapidly, before slowing down as it nears the top of the fluid domain and converges on the surface, $y_p/D = 1$.

Table 3. Summary of the four stages of the life cycle of a plume, and details of the start times and durations of each stage in the current experiments.

Stage	Start time	Duration	Behaviour
Formation	0 min	12.1 min	Plume forms near base
Rising	12.1 min	58.7 min	Plume rises through fluid
Spreading	70.7 min	59.9 min	Plume head spreads at surface
Declining	130.6 min	∞	Temperatures gradually decline

On the basis of Fig. 2, the lifespan of the isolated plume can be broken down into four stages, which are indicated in Fig. 2 by the grey lines; the Formation Stage, in which the plume forms but remains close to the heater; the Rising Stage, in which the plume rises through the fluid; the Spreading Stage, in which the plume has reached the top of the fluid domain and the stem continues to transfer heat from the base to the surface; and the Declining Stage, after the heater has been turned off and the temperature at the base of the stem falls. The details of the four stages of the life cycle of the plume are summarized in Table 3. The onset of the Rising Stage was taken as the point at which the acceleration of the plume height reached a maximum, at $t = 12.1$ min and $y_p = 18.2$ mm, and the stage ended when the plume reached the thermocouple near the fluid surface. The rise time of the plume is equal to the length of this stage, $\tau_r = 58.7$ min.

The behaviour of the fluid in the Formation Stage is likely to be dependent on boundary conditions such as the size of the heater and the time taken to reach the applied temperature. The last factor will vary significantly between studies; in numerical studies it is common to apply an instantaneous increase in the heater temperature at

$t = 0$ (e.g. Farnetani & Samuel 2005; Lin & van Keken 2006; Whitehead *et al.* 2013); in experiments this is not possible, and all heaters will have a finite rise time; while in the mantle the formation of a plume occurs due to a local perturbation to the thermal boundary layer rather than an applied change in the temperature. Therefore, the Formation Stage in the current experiments is of limited interest to the general study of thermal and mantle plumes, and will not be discussed further. The other three stages are relevant to the case of the mantle and ideal thermal plumes (regardless of how they are formed) and are described in detail in the following sections.

3.2 Rising Stage

Figs 3(a)–(f) show the tracer and the corresponding σ_f^- fields at three points in the Rising Stage, as the plume moves through the fluid domain. The white circular symbol above the plume represents the point at which the thermocouple measured the surface temperature. The non-dimensional temperature signal at this point is shown in Fig. 3(g), with the symbols indicating the times shown in Figs 3(a–f). The colours in the tracer fields (Figs 3a, c and e) denote the height from which each tracer originated at $t = 0$. White regions correspond to points in the flow where the local tracers originated from outside the PIV domain, typically from the layer between the bottom surface of the tank and the lowest row of PIV measurements ($y = 0-1.73$ mm). There are also some white regions at the lower right and left sides of the tracer fields due to the large-scale convection induced by the plume; as the fluid above the heater rises, other fluid is drawn into the PIV domain from either side to replace it. The white region at the bottom right is typically larger than that on the left, because the plume is not aligned with the centre of the PIV domain.

The σ_f^- fields in Figs 3(c), (d) and (f) correspond to the attracting structures in the flow, which separate qualitatively distinct parts of the flow. A general description of the σ_f^- fields associated with a rising thermal plume has been provided elsewhere (Cagney *et al.* 2015) and are only briefly discussed here. In this case, the σ_f^- fields contain two distinct LCSs; a vertical line along the stem (separating the flow on either side of the axis of symmetry) and an arc which corresponds to the boundary of the plume head. The corresponding tracer fields show that the fluid above the arc is ambient fluid, while below the arc the fluid originated from near the bottom surface of the tank (the dark blue and white regions in Figs 3a, c and e) and has been raised by the plume.

When the plume is relatively low in the fluid ($y_p \approx 100$ mm, Figs 3a and b) the plume head appears to be circular. However, as the head continues to rise, it begins to flatten (Figs 3c and d) while the stem appears to maintain the same thickness. At late stages (Fig. 3f), the σ_f^- fields reveal characteristic scrolls at the edges of the plume head. However, they are relatively insignificant in size compared to the flow visualization images of (Griffiths & Campbell 1990), who injected buoyant low-viscosity fluid into syrup, which suggests that thermal plumes may 'stir' the flow less than some injection experiments suggest. The implications of this are discussed further in Section 6.

In each of the three pairs of tracer and σ_f^- fields shown in Fig. 3, the temperature near the surface of the fluid has not shown any significant increase (Fig. 3g). This is because the heat transfer occurs predominantly by convection; therefore the Θ_S signal should not show any significant increase until the plume reaches the thermocouple. However, despite the large *Pe*, heat conduction is not negligible (this after all is how the fluid gains heat from the heater).

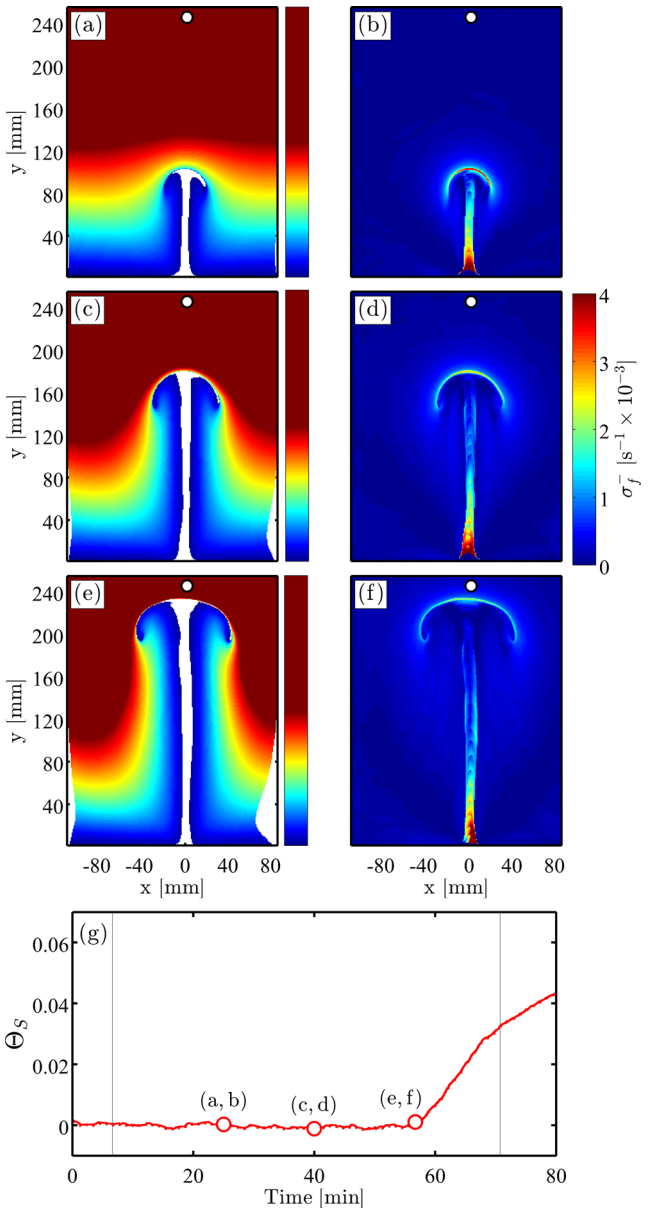

Figure 3. Tracer fields (a, c, e) and σ_f^- fields (b, d, f) calculated at three points in the Rising Stage; $t = 25$ min (a, b), $t = 40$ min, (c, d) and $t = 56.7$ min (e, f). The colours in the tracer fields denote the height from which each tracer originated from when the heater was turned on, with the white regions denoting points where the local fluid originated from outside the PIV domain. The non-dimensional temperature signal near the surface is shown in (g), with the symbols denoting the times at which the various fields were calculated.

This conduction causes the plume to be surrounded by a 'thermal halo' which is larger than the plume head identified by the tracer fields and the arc-like ridges in the σ_f^- fields.

This effect is apparent in Fig. 3(e); the temperature near the surface begins to rise at this point ($t = 56.7$ min in Fig. 3g) although the plume has not yet reached the thermocouple, and the material around the thermocouple has not originated from near the heater. Therefore, the increase in Θ_S can be attributed to the arrival of the thermal halo at the sensor. The height of the plume at this point is 233.4 mm, indicating that the thermal halo extends 12 mm ahead of the plume.

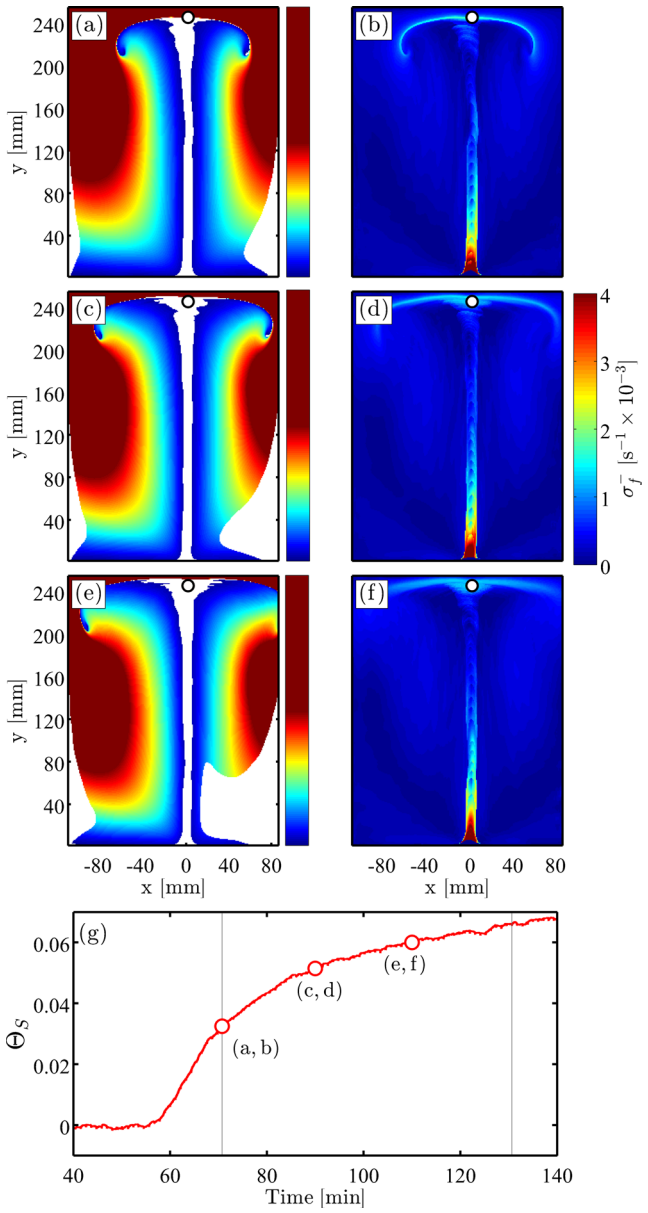

Figure 4. Tracer fields (a, c, e) and σ_f^- fields (b, d, f) calculated at three points in the Spreading Stage; $t = 70.73$ min (a, b), $t = 90$ min, (c, d) and $t = 110$ min (e, f). The colours in the tracer fields denote the height from which each tracer originated from when the heater was turned on, with the white regions denoting points where the local fluid originated from outside the PIV domain. The non-dimensional temperature signal near the surface is shown in (g), with the symbols denoting the times at which the various fields were calculated.

3.3 Spreading Stage

The Spreading Stage is defined at $t = 70.73$–130.62 min, which corresponds to the point at which the plume head reached the thermocouple to the time at which the heater was turned off. During this time the head flattens to form a 'pancake' (Griffiths & Campbell 1991; Ribe & Christensen 1994; Ballmer *et al.* 2011) that gradually spreads at the surface. Tracer and σ_f^- fields are shown in Figs 4(a)–(f) at three instances in the Spreading Stage, along with the corresponding surface temperature signal in Fig. 4(g).

The fields in Figs 4(a) and (b) correspond to the point at which the plume first reaches the thermocouple. The arrival of the plume does not coincide with a sudden change in Θ_S. This is likely to be caused by two related effects; the earlier increase in Θ_S since the arrival of the thermal halo, and the cooling of the material raised from very deep in the fluid domain.

Over the course of the Spreading Stage, Θ_S increases from 0.032 to 0.066. Despite the surface temperature doubling in this stage, the changes to the tracer and σ_f^- fields are relatively small. The most notable change in these fields with time is the gradual broadening of the plume pancake, which is apparent from the width of the σ_f^- arc and the material of deep origin (dark blue) in the tracer fields near the top of the fluid domain. There is also a notable increase in the amount of material in the tracer fields which has originated from outside the PIV domain. This is apparent in the lower half of Fig. 4(e), particularly on the right-hand side where the edge of the PIV domain is relatively close to the plume.

3.4 Declining Stage

The Declining Stage starts at the point at which the heater is turned off ($t = 130.6$ min), and it continues indefinitely, although no PIV measurements are acquired for $t > 194.6$ min. As in the previous two sections, Figs 5(a)–(f) show tracer and σ_f^- fields acquired at three instances in this stage, with the non-dimensional temperature signal near the surface shown in Fig. 5(g).

The basic structure of the σ_f^- fields is essentially the same as that observed in the Spreading Stage; a thin stem of elevated σ_f^- is present along the plume axis, where the tracers have originated from very deep in the PIV domain, and the spreading pancake is present at the surface. In this case, the pancake has spread so wide that it extends beyond the PIV domain. As the heat input and the source of buoyancy gradually decline, so too does the magnitude of the velocity within the flow, leading to a reduction in the magnitude of σ_f^- field with time. This is particularly evident at the base of the stem in Figs 5(b), (d) and (f). As in previous sections, Fig. 5 does not indicate that any significant amount of ambient material from above the base of the fluid domain (green and yellow regions) has been brought close to the surface. This supports the views that the geochemical signal associated with OIBs is derived from the deep mantle (Hart *et al.* 1992) and that in at least some cases, such as the Samoan plume, plumes may contain material from ancient subducted slabs which now lie at the base of the mantle (White 2010).

The signal in Fig. 5(g) does not immediately decline until some time after t_{co}. The 'time lag' is discussed further in Sections 4 and 6.

3.5 Rise velocity

The rise velocity of material in a mantle plume is one of the crucial factors in determining whether or not the plume will cause volcanism at the surface (along with other factors including the lithospheric thickness and the chemical composition of the plume material). The material in the plume cools as it rises through the fluid domain; if the rise velocity is sufficiently high the material does not have time to cool and may undergo decompression melting. However, if the rise velocity is too low the material temperature may decline faster than the solidus and the plume will not cause significant melting. The rise velocity of plumes in the mantle is also important in terms of understanding the heat flow in the mantle, the temporal variations in the heat flux out of the core (Lay *et al.* 2008), the timescales of mantle convection and the rate of mantle mixing (Kellogg 1992). The rise velocity of the plume is readily available

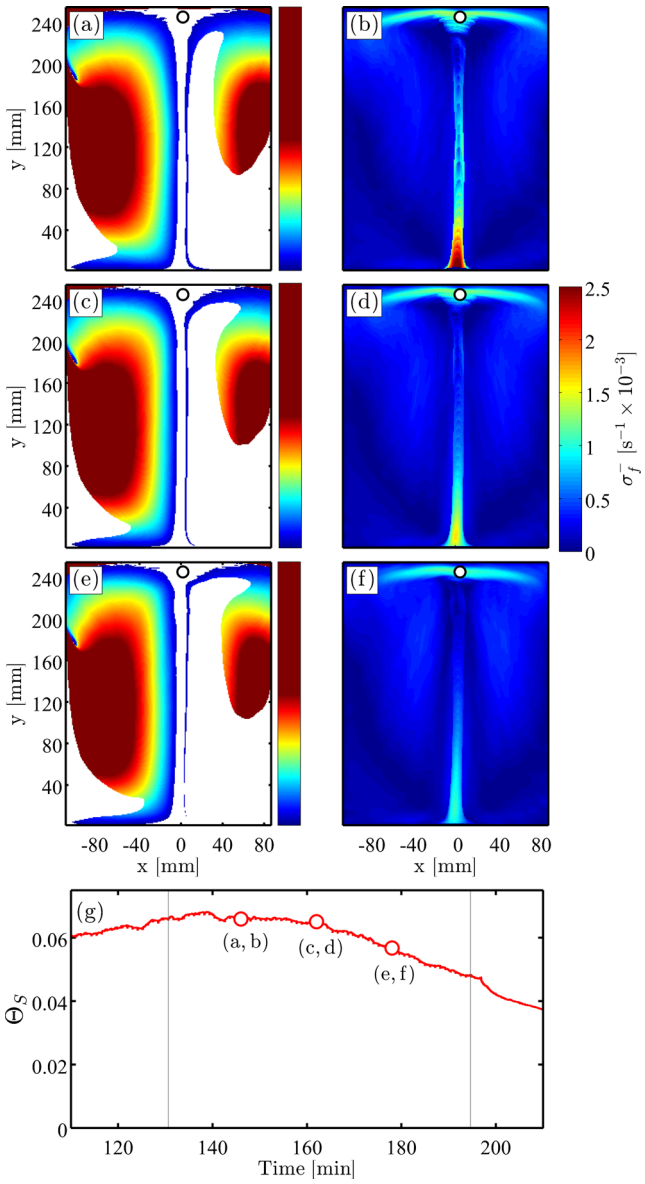

Figure 5. Tracer fields (a, c, e) and $\overline{\sigma_f}$ fields (b, d, f) calculated at three points in the Declining Stage; $t = 146$ min (a, b), $t = 162$ min, (c, d) and $t = 178$ min (e, f). The colours in the tracer fields denote the height from which each tracer originated from when the heater was turned on, with the white regions denoting points where the local fluid originated from outside the PIV domain. The non-dimensional temperature signal near the surface is shown in (g), with the symbols denoting the times at which the various fields were calculated.

from the tracer fields discussed in the previous sections. The height of the plume shown in Fig. 2(c) was found by measuring the highest point at $x = 0$ at where the material originated from $y \leq 1.73$ mm at $t = 0$. This can also be performed for later times, t_i, by advecting the tracers backwards in time until t_i (rather than until $t = 0$). In this manner the rise velocity can be calculated for material released from the base of the plume stem at any point throughout the plume's life cycle. The velocities are largest at the plume axis, and therefore these signals correspond to the *maximum* rise velocity across the width of the plume.

Fig. 6(a) shows the rise trajectories of material originating near the heater ($y \leq 1.73$ mm) at various times. The symbols denotes from which of the four stages of the plume's life cycle each tra-

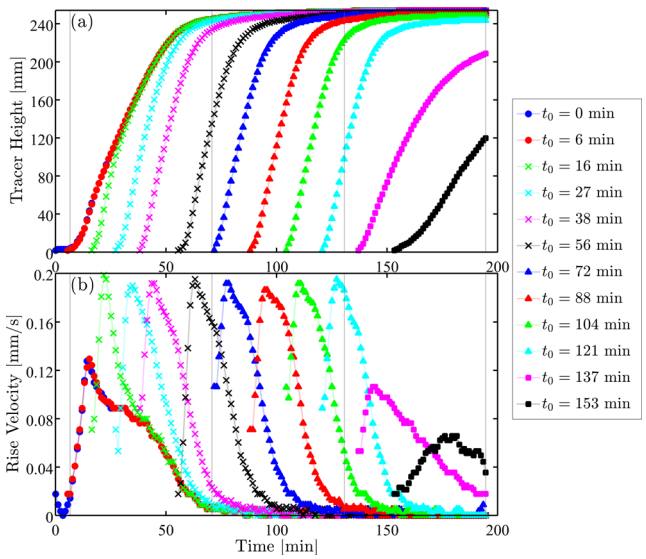

Figure 6. Variation in the height of numerical tracers released at various times throughout the life cycle of the plume (a), and the corresponding rise velocity of the trajectories (b). The symbols denote in which stage the trajectory starts in; Formation Stage, circles; Rising Stage, crosses; Spreading Stage, triangles; Declining Stage, squares.

jectory begins. The two trajectories starting in the Formation Stage (red and blue circles) are very similar, despite starting at early and late points in the stage. Both trajectories remain level until the onset of the Rising Stage, at which point they rise sharply before converging slowly towards the surface of the fluid. The trajectory of the material at the base of the plume calculated slightly later, at $t = 16.4$ min (when the plume has reached $y_p = 52.2$ mm, green crosses) begins to rise immediately and catches up with the earlier trajectories, before appearing to follow the same convergence path to the fluid surface. This suggests that the material at the heater at $t = 16.4$ min rises rapidly through the stem and accumulates in the plume head. Trajectories starting at later times in the Rising and Spreading Stages (crosses and triangles, respectively) are all similar, being characterized by an immediate and rapid rise, followed by a slow convergence towards the surface. The trajectories starting in the Declining Stage (squares) also increase steadily with time, but they do so at a slower rate and have not reached the surface by the time the final PIV field was acquired.

One might expect from visual inspection of the trajectories shown in Fig. 6(a) that the rise velocity is approximately constant, as suggested by previous studies. Indeed, fitting a linear regression to the trajectories has been used to estimate the average rise velocity of the plume throughout its ascent in previous studies [including by the present authors (Cagney *et al.* 2015)]. However, the high temporal resolution of the measurements in this study allows the rise velocity signals to be measured as a function of time, $u_r(t)$, and the plume dynamics to be studied in more detail. The rise velocity signals of the trajectories were calculated using the least-squares method, and are shown in Fig. 6(b). The signals starting in the Formation Stage are again very similar, reaching a maximum of 0.13 mm s^{-1} at $t =$ 15.3 min, before decreasing monotonically to zero as the trajectories near the surface. By $t \approx 40$ min, the first rise velocity signal of the Rising Stage (green crosses) matches the earlier signals from the Formation Stage. This is approximately the same point at which these three trajectories coalesced in Fig. 6(a), confirming that all material released at approximately $t < 20$ min accumulates in the plume head and reaches the surface at approximately the same time.

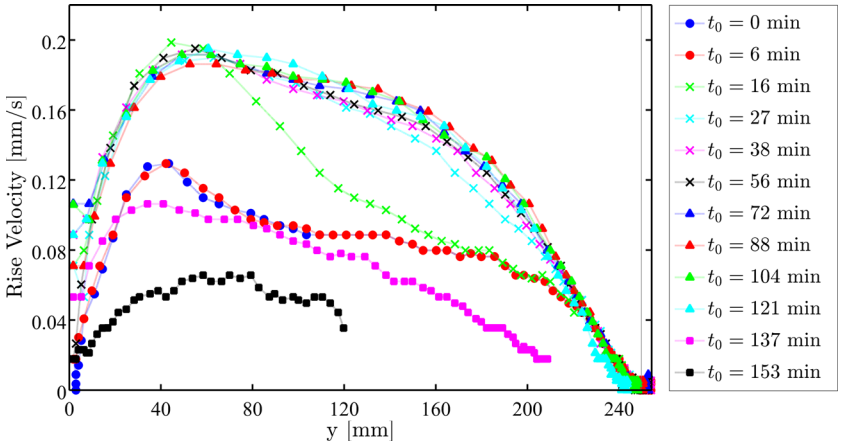

Figure 7. Rise velocity of tracer trajectories released at various points in the life cycle of the plume as a function of the tracer height. The rise velocity signals (and the corresponding trajectories) are shown in Fig. 6 as a function of time. The symbols denote in which stage each of the trajectories start in; Formation Stage, circles; Rising Stage, crosses; Spreading Stage, triangles; Declining Stage, squares.

The rise velocity signals in the Rising and Spreading Stages all exhibit very similar characteristics; the velocity increases sharply to 0.19–0.2 mm s^{-1}, undergoes a brief period in which the velocity declines at an apparently constant rate, and then converges quickly to zero. The increase in the maximum rise velocity of the trajectories released after $t \gtrsim 20$ min can be explained in terms of the temperature-dependence of the fluid rheology. When the trajectories are part of a plume head which is rising through ambient cold material (i.e. the trajectories released before $t \approx 20$ min, which accumulate in the plume head) they encounter high viscous drag which reduces the rise velocity. However, for trajectories starting at later stages, the tracers are passing through material which has already been heated and therefore has a lower viscosity and provides a weaker drag force. Furthermore, these later trajectories do not lose as much heat to ambient material (which is now hotter than in the Formation Stage) and do not have to use energy moving the ambient material above the tracer out of the way (since this material is now also rising), both of which would cause the material to have a lower rise velocity.

The signals starting in the Declining Stage are less well organized, most likely as a result of the progressively declining source of buoyancy. They also rise to a local maximum (albeit quite slowly for the last case) before beginning to fall. The maximum rise velocities observed in this stage are considerably lower than those observed in the Rising and Spreading Stages.

Moses *et al.* (1993) used shadowgraphs to measure the height of thermal plumes, and stated that the plumes rise at a constant velocity (although they do not show the measured trajectories as a function of time). Coulliette & Loper (1995) also observed the rise velocity of a thermal plume to be roughly constant after a brief period of acceleration, provided the viscosity contrast was not excessively large ($\mu_{max}/\mu_{min} < 10^8$). In contrast, the trajectories released in the Formation Stage (which correspond to the height of the rising plume head) only undergo a brief period of constant rise velocity at $t \approx 25.1$–31.6 min. This corresponds to the period in which the plume head passes through the centre of the fluid domain, $y_p/D \approx 0.41$–0.54. At greater plume heights, the plume decelerates as it nears the fluid surface. The reduction in the rise velocity at various heights is likely to be influenced by the proximity of the plume to the boundaries of the fluid domain, and it is possible that if the vertical extent of the fluid domain is greater, the range over which the plume has a near-constant rise velocity will increase. However, the data in Fig. 6 indicate that the rise velocity is strongly dependent on the position of the plume in the fluid domain; this factor was also addressed by van Keken *et al.* (2013), but has not been taken into account in various analytical and empirical models (Griffiths & Campbell 1990; Moses *et al.* 1993; Coulliette & Loper 1995).

This dependency is shown in Fig. 7, which presents the rise velocity signals shown in Fig. 6(b) as a function of the tracer height. The rise velocity signals which start in the Formation Stage are closely aligned, and are lower than those released in the Rising and Spreading Stages, as in Fig. 6(b). In all cases (excluding the signals starting in the Declining Stage) the velocity reaches a maximum in the region $y \approx 40$–65 mm above the heater, i.e. at approximately 15–25 per cent of the height of the fluid domain. The velocity signals of all the trajectories released before the Declining Stage coalesce near the surface, for $y \gtrsim 220$ mm.

4 EFFECT OF RAYLEIGH NUMBER

Fig. 8 shows the tracer fields at $y_p = 200$ mm for the three experiments. The morphology of the plume appears similar in each case, although the head is slightly narrower at high temperatures (Figs 8b and c). The viscosity contrast caused by the temperature-dependence of the syrup viscosity acts to increase the size of the plume head (Kellogg & King 1997), i.e. the opposite effect to the trend observed here. Therefore, the changes in the diameter of the plume head are a result of the increasing Rayleigh number, rather than the rheology. In contrast to the head, the diameter of the plume stem does not appear to change significantly over this *Ra* range, as can be seen in the profiles of the tracers fields shown in Fig. 9.

The temperature signals measured at the surface for the three experiments are shown in Fig. 10(a). For ease of comparison, the time is normalized by the rise time measured for each experiment, and the profiles are lightly shaded during the respective Declining Stages. The trend in each case is qualitatively similar; the temperature is approximately constant until $t/\tau_r \approx 1$, when the plume reaches the thermocouple; the temperature then increases rapidly before stabilizing in the range $\Theta_S \approx 0.05$–0.07; following the heater being switched off the temperature appears to remain constant for a brief period before declining exponentially. The magnitude of the non-dimensional temperature signal is greater for the high ΔT cases, implying that plumes transfer heat to the surface more efficiently

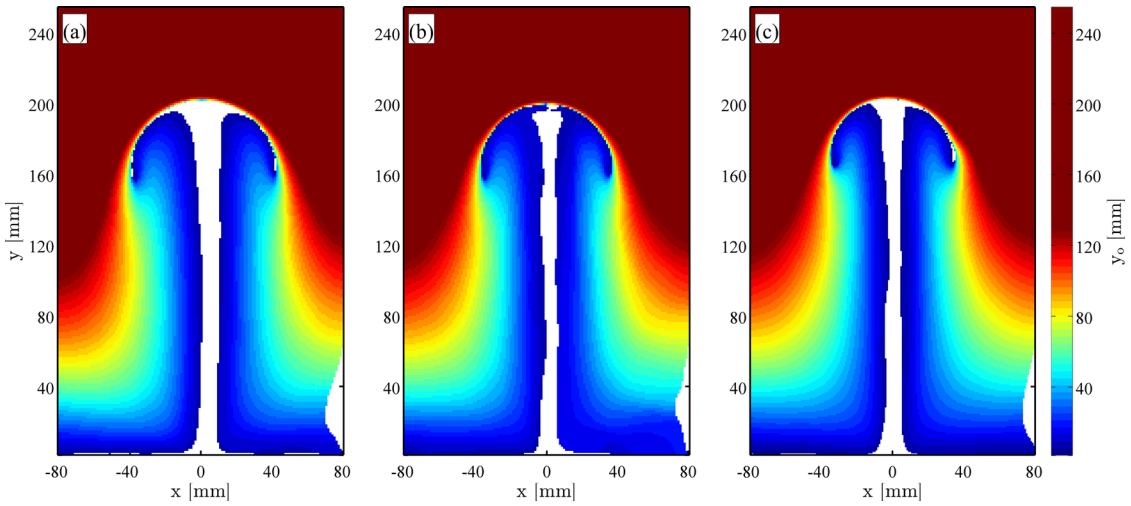

Figure 8. Tracer fields acquired at $y_p = 200$ mm, for $Ra = 4.4 \times 10^5$ (a), 5.48×10^5 (b) and 6.4×10^5 (c).

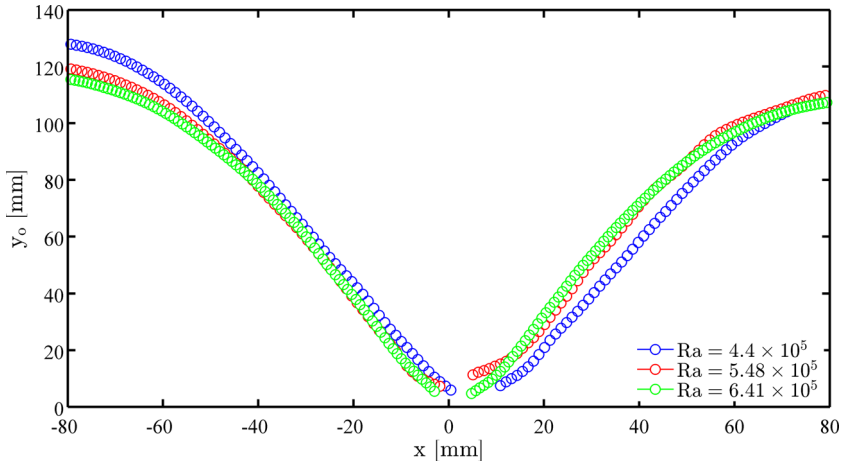

Figure 9. Profiles of the tracer fields at $y = 100$ mm, when the plume height was $y_p = 200$ mm, for the three experiments. The entire tracer fields are shown in Fig. 8.

at higher *Ra*. The cause and implications of this effect is studied in more detail in the following section.

The temperature signals following the cut-off time are shown in Figs 10(b) and (c). The heater temperature is here normalized by the peak temperature, $\Theta_{S,p}$ (taken as the temperature measured over the period $\tau_r/3$ after $t_{\rm co}$). The basic features of the temperature signals in this stage are again very similar; the temperature remains approximately constant for a period, $\tau_{\rm lag}$, before declining exponentially (which appears as a straight line in Figs 10b and c). The temperature signals in the Declining Stage can be modelled as:

$$\log_{10}\left(\frac{\Theta_S}{\Theta_{S,p}}\right) = \begin{cases} 0, & \text{if } t - t_{\rm co} < \tau_{\rm lag} \\ -r_D(t - t_{co} - \tau_{\rm lag}), & \text{if } t - t_{\rm co} \geq \tau_{\rm lag}, \end{cases} \quad (6)$$

where r_D is the rate of decline or cooling near the surface The dashed black lines in Fig. 10(b) show the best fit of each of the temperature signals to eq. (6). The resulting estimates of $\tau_{\rm lag}$ and r_D (Table 4) are discussed in the following sections.

Fig. 10(c) shows the same temperature signals in the Declining Stage, with time now normalized by the rise time. The three signals collapse, showing that the dynamics in the Declining Stage are controlled by the same timescale as the Rising Stage (i.e. τ_r).

5 TIME LAG UNDER MANTLE CONDITIONS

It is interesting to note that the time lag is less than the rise time of material in the plume stem, $\tau_{\rm lag}/\tau_{r,S} \approx 0.6$ (Table 4). This would not be the case if heat transport occurred by convection alone, and suggests the possibly significant role of conduction in determining $\tau_{\rm lag}$. Given the high Peclet number in the mantle, and the correspondingly weak role of conduction in mantle plumes, we briefly consider in this section how $\tau_{\rm lag}$ would vary in the absence of conduction, and what $\tau_{\rm lag}/\tau_{r,S}$ relationship we may expect to occur in the mantle.

The temperature evolution along the plume axis is controlled by the heat equation

$$\frac{\partial T'}{\partial t} = -\mathbf{u}\cdot\nabla T' + \kappa\nabla^2 T', \quad (7)$$

where $T' = T - T_{\rm amb}$, and $\mathbf{u}$ is the velocity vector. If the plume is axisymmetric (with $r = 0$ at the plume axis), eq. (7) reduces to:

$$\frac{\partial T'}{\partial t} = -u_y\frac{\partial T'}{\partial y} + \kappa\left(\frac{1}{r}\frac{\partial}{\partial r}\left(r\frac{\partial T'}{\partial r}\right) + \frac{\partial^2 T'}{\partial y^2}\right), \quad (8)$$

where y and u_y is the vertical dimension and velocity along the plume stem, respectively. The length-scale of conduction is given

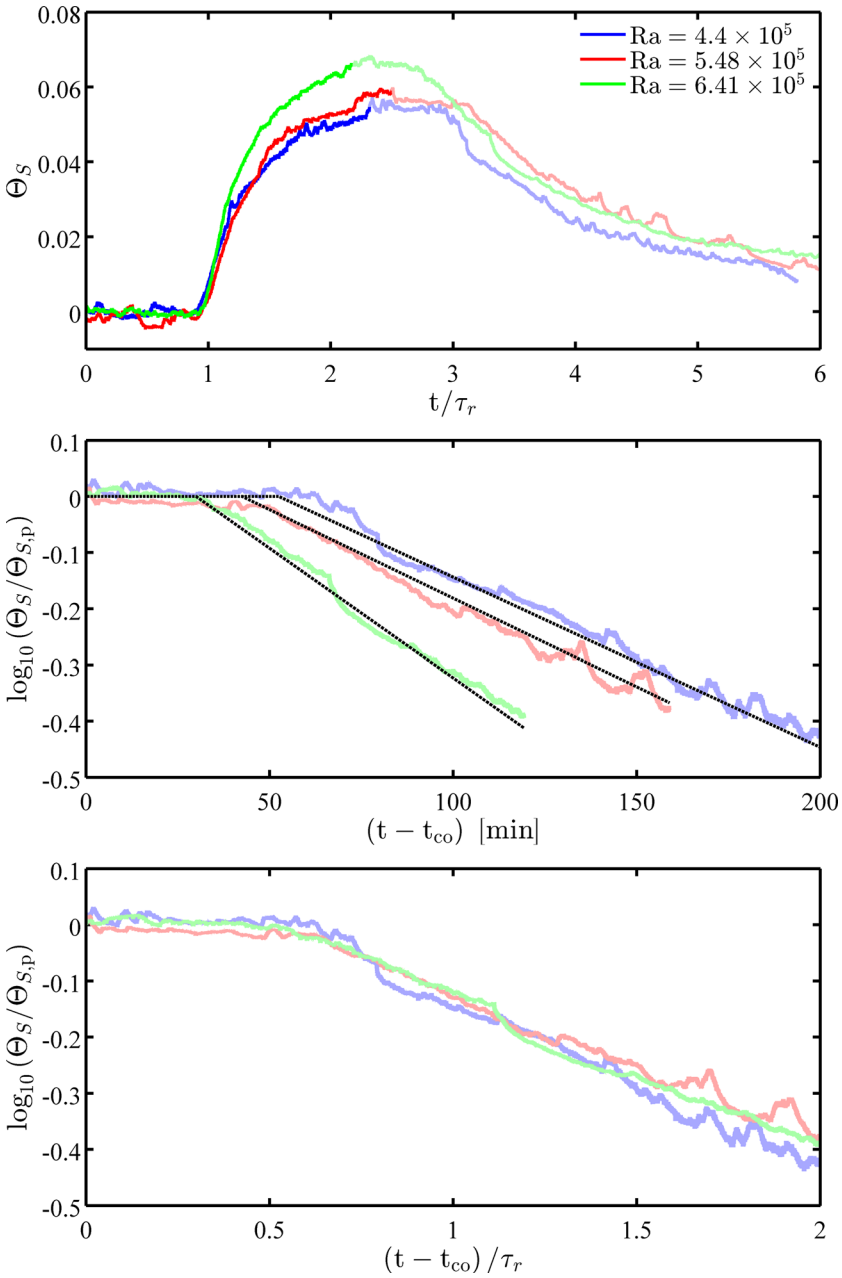

Figure 10. Temperature signals measured at the surface for the three experiments; the temperature signals throughout the plume life cycle, with the dark regions of the lines denoting points before the heat was turned off, and the lightly shaded points denote points in the Declining Stage (a); the temperature signals in the Declining Stage with the best fit to eq. (6) (b); the temperature signals in the Declining Stage with time normalized by the rise time (c).

by $\ell = \sqrt{\kappa \tau_{r,S}}$. Assuming that the rise time of material in a plume stem during the Spreading Stage is of the order of 50 Ma (equivalent to a mean rise velocity of approximately 5 cm a^{-1}), this corresponds to $\ell = 12.8$ km, which is significantly less than the length-scale of convection (∼2890 km). Therefore, the role of conduction is negligible and the κ term in eq. (8) can be neglected.

We now require an estimate of u_y. It is reasonable to assume that the local rise velocity is proportional to the local buoyancy, i.e. the velocity is proportional the rise velocity of a Stoke's sphere:

$$u_y = \frac{f \alpha g \delta^2}{\mu} T', \tag{9}$$

where f is a constant and δ is the nominal diameter of the Stoke's sphere. In practice, the value of $f\delta^2$ is likely to be a function of the Rayleigh number; however, for our current considerations the choice of $f\delta^2$ is arbitrary, and does not affect our results (as will be shown later). We take μ in eq. (9) to be equal to the ambient viscosity, which controls the rise velocity of plumes (Moses *et al.* 1993). The contrast between the ambient viscosity and the viscosity in the hot plume stem, $\gamma = \mu_{\max}/\mu_{\min}$, may have a weak effect on the rise velocity. According to previous studies (White & Luther 1975; Griffiths 1986; Davaille *et al.* 2011), the viscosity contrast should cause the rise time to be deducted relative to the isoviscous case by a factor of

$$\frac{\tau_r}{\tau_{r,\text{isoviscous}}} = \frac{5}{4} \frac{\gamma + 1}{\gamma + 3/2}. \tag{10}$$

Table 4. Summary of the timescales of the plume life cycle and some other parameters. See the text for a discussion of the various ratios presented.

Parameter	Experiment 1	Experiment 2	Experiment 3
Ra	4.4×10^5	5.48×10^5	6.4×10^5
$\Theta_{S,\,\max}$	0.0534	0.0576	0.0655
τ_r	100 min	79.4 min	59.6 min
$\tau_{r,\,S}$	87.1 min	68.6 min	51.5 min
$\tau_{\rm lag}$	52.4 min	42.3 min	29.9 min
r_D	30.5 $\rm min^{-1}$	19.9 $\rm min^{-1}$	16.4 $\rm min^{-1}$
$\tau_{r,\,S}/\tau_r$	0.868	0.863	0.864
$\tau_{\rm lag}/\tau_r$	0.522	0.533	0.502
$\tau_{\rm lag}/\tau_{r,\,S}$	0.602	0.617	0.581
$r_D\tau_r$	0.304	0.25	0.275
$\Theta_{S,\,\max}\tau_r$	5.26 min	4.58 min	3.91 min

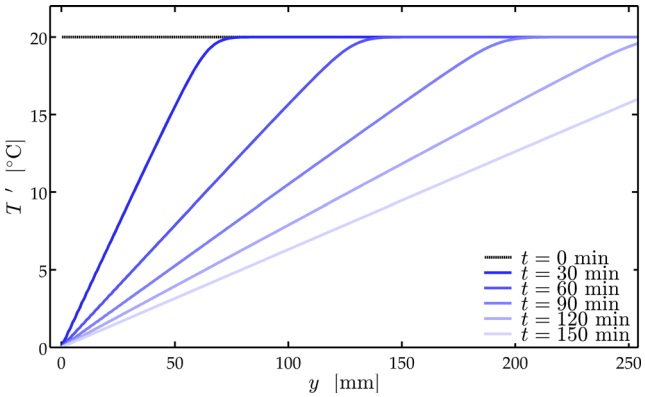

Figure 11. Temperature profiles at various times found by numerically solving eq. (11), for $\Delta T = 20\,^\circ$C and $f\delta^2 = 300$.

For $\gamma \geq 25$, the effect of any further increases in γ are less than 2 per cent. We can therefore neglect the effect of the temperature-dependent rheology in our analysis, and allow any effect of eq. (10) to be accounted for through our choice of $f\delta^2$.

Combining eqs (8) and (9), we find

$$\frac{\partial T'}{\partial t} = -\frac{f\delta^2 \alpha g}{\mu} T' \frac{\partial T'}{\partial y}, \tag{11}$$

which can be solved numerically to predict the evolution of the temperature along the plume axis. Eq. (11) was solved numerically for conditions similar to the experimental values (i.e. the same fluid properties and over the range $y = 0$ to 256 mm). The initial temperature was set to $T(y) = \Delta T$ along the axis, and then the temperature at $y = 0$ was set to zero for $t > 0$.

Temperature profiles found for $\Delta T = 20\,^\circ$C ($Ra = 2.7 \times 10^5$) and $f\delta^2 = 300$ are shown in Fig. 11. The time lag was taken as the difference between the times at which the heat source was removed and the temperature at $y = 246$ mm (the height of the thermocouple) had declined by 1 per cent. The variation in $\tau_{\rm lag}$ is shown in Fig. 12(a) over a temperature range of $\Delta T = 20{-}45\,^\circ$C ($Ra = (2.7{-}6.1) \times 10^5$) for two choices of $f\delta^2$. In both cases, the time lag decreases with increasing Ra.

The steady-state rise time is equal to D/u_y at $t = 0$ (where $u_y = f\delta^2\alpha g \Delta T/\mu$). Fig. 12(b) shows the dependence of τ_{lag} on $\tau_{r,\,S}$; for both choices of $f\delta^2$ and for all Ra, the time lag is given by

$$\tau_{\rm lag} = 0.937\tau_{r,S}. \tag{12}$$

The constant of proportionality is close to unity, and higher than the value predicted from the experiments (red squares in Fig. 12b). This indicates that in the experiments the reduction in $\tau_{\rm lag}$ with respect to $\tau_{r,\,S}$ is primarily (but not entirely) caused by conduction in the test-section, and that in the mantle (where the role of thermal diffusion is weak) the true time lag is likely to be controlled by eq. (12). The fact that the linear relationship between τ_{lag} and $\tau_{r,\,S}$ was observed both experimentally and in the results of the simple model, and that it did not depend on the choice of $f\delta^2$, suggests that the relationship between the two variables is robust and is not dependent on the Rayleigh number (although it appears to be affected by the presence of conduction).

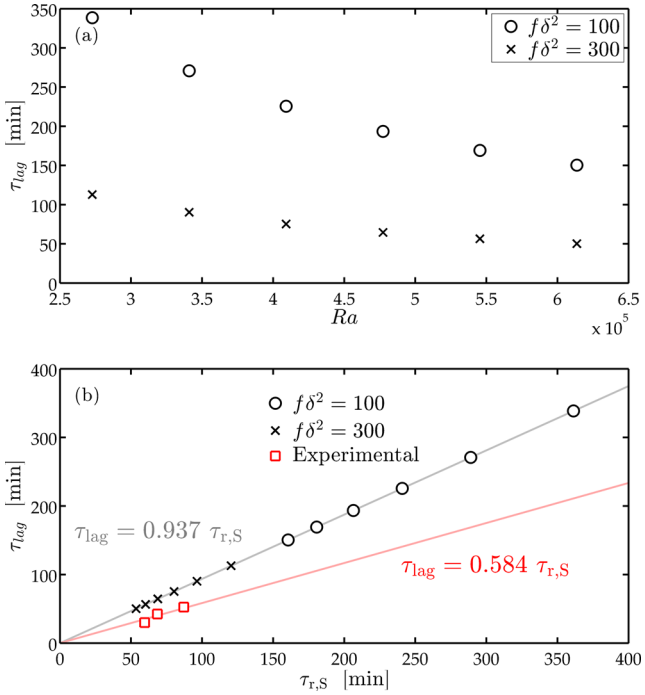

Figure 12. Variation in the predicted time lag of plumes as a function of Rayleigh number (a) and the rise time (b), for two choices of $f\delta^2$. The values were found by numerically solving eq. (11), as described in the text, while the experimental values (red squares) are taken from Table 4. The choice of $f\delta^2$ does not affect the scaling of $\tau_{\rm lag}$ with $\tau_{r,\,S}$.

6 DISCUSSION

Table 4 lists some key parameters and timescales associated with the three experiments, including the maximum non-dimensional temperature recorded near the surface, the rise times in the Rising and Spreading Stages, the time lag between the heater being switched off and the surface temperature beginning the decline, and the rate of this decline.

Both τ_r and $\tau_{r,\,S}$ decrease with increasing Rayleigh number, as is expected from previous experimental studies (e.g. Moses *et al.* 1993; Bercovici & Mahoney 1994; Cagney *et al.* 2015). The rise time is lower in the Spreading Stage as a result of thermal and rheological effects discussed in Section 3.5. Table 4 shows that the ratio between the two times scales is approximately constant, with $\tau_r/\tau_{r,\,S} \approx 0.865$. This remarkable consistency of this ratio across the three experiments implies that the rise time during the Rising Stage is not significantly affected by the size of the plume head; if this was the case, the ratio would change as the plume head is smaller at high Rayleigh numbers (Fig. 8).

This also suggests that the material erupted in volcanic chains will have experienced less thermal (and chemical) diffusion than the material in LIPs. However, the relative difference between $\tau_{r,\,S}$

and τ_r is insignificant compared to the uncertainty in estimates of either variable under mantle conditions based on theoretical or geochemical arguments (Campbell 2005; White 2010), and is unlikely to be measurable in practice.

It is significant that τ_{lag}/τ_r and $r_D\tau_r$ are also approximately constant for the three experiments (as can be seen in Fig. 10c), with $\tau_{\rm lag}/\tau_r \approx 0.52$ and $r_D \approx 0.27/\tau_r$. This implies that a single timescale governs the Rising, Spreading and Declining Stages of the plume's life cycle, which considerably simplifies the scaling of the timescales of plume dynamics. For example, if the rise time of mantle plumes can be constrained (either in the Rising or Spreading Stages), it will also be possible to predict the time lag between the depletion of the plume source and the reduction in excess temperature at the surface and the rate of this cooling. The importance of a single timescale throughout the entire life cycle of a plume is also supported by the observation in the previous section that under mantle conditions (weak thermal diffusion), τ_{lag} remains proportional to $\tau_{r,S}$ (and therefore also to τ_r) regardless of the Rayleigh number (eq. 12).

Following the initial depletion of a plume source, the time taken for the excess temperature to decline to a factor f of its original value (neglecting the role of the overriding plate motion) can be found by rearranging eq. (6):

$$t_f = \tau_{\rm lag} - \frac{\log_{10} f}{r_D}. \tag{13}$$

Taking into account eq. (12) and the values of r_D in Table 4, this is equivalent to

$$t_f = 0.937\tau_{r,S} - \frac{\log_{10} f}{0.27}\tau_r = \left(1.08 - \frac{\log_{10} f}{0.27}\right)\tau_r. \tag{14}$$

If we again assume that the rise time of material in a plume in the Spreading Stage to be 50 Ma (which is equivalent to $\tau_r = 43.25$ Ma), then it will take of the order of ~47 Ma for the excess temperature and volcanism at the surface hotspot to begin to decline, and ~206 Ma before the excess temperature at the hotspot has declined to 10 per cent of its peak value ($f = 0.1$). In practice, this period may be reduced by the effects of plate motion, which we do not examine in this work, but this suggests that the thermal source of a plume may be depleted for a significant fraction of the plume's apparent life cycle (i.e. the period of time in which it causes a hotspot at the surface). Eqs (6) and (13) also suggest that reduction in excess temperature over the last 20 Ma at the Louisville hotspot (Lonsdale 1988) may therefore be the result of the depletion of the plume source which began ~67 Ma ago.

The maximum temperature increase at the surface, $\Theta_{S,\max}$ also increases with Rayleigh number, as can be seen in Fig. 10(a). The exact values of $\Theta_{S,\max}$ should be treated with some caution, as unlike other parameters discussed here, $\Theta_{S,\max}$ may depend on the duration of the Spreading Stage relative to the rise time; however, the general trend of increasing $\Theta_{S,\max}$ with heater temperature appears to be robust. The increased efficiency of heat transfer with Rayleigh number has important implications for mantle convection, such as predicting the difference between the excess temperature of plumes which form in the lower or upper mantles (where *Ra* differs by up to an order of magnitude, Table 2). The increased efficiency cannot be explained solely in terms of a change in the rise time (which would allow less time for radial heat loss from the plume stem); if this was the case the product $\Theta_{S,\max}\tau_r$ would be constant. In fact, Table 4 shows that there is considerable variation in this parameter, indicating that the variation in the excess temperatures and melting induced by plumes in the mantle is not controlled by their rise time (although this may still play a role).

When the plume reaches the thermocouple near the fluid surface, the non-dimensional temperature signal (Fig. 4g) does not indicate a dramatic change. In general, the smoothness of the temperature signal suggests that the temperature field is diffuse and varies smoothly in space. However, the Peclet number is higher in the mantle, implying that the influence of the thermal diffusion is weak. This is likely to lead to a relatively small thermal halo surrounding the plume. For example, Griffiths & Campbell (1991) argue that as a mantle plume reaches the lithosphere, the thermal halo should extend only a few km above the top of the plume. If this is the case, the arrival of the plume at the base of the lithosphere will be marked by a sharper increase in surface temperature, which may be apparent in the geological record. The question of how the arrival of a plume at the lithosphere affects the surface temperature and volcanism is one of the most poorly understood aspects of mantle plumes dynamics, and is closely related to the question of why some volcanic chains originate at an LIP, while many others do not (Courtillot *et al.* 2003).

The tracer fields shown in Figs 3–5 indicate that the plumes do not entrain significant amounts of material into the scrolls in the head as suggested by the early flow visualization work of Griffiths & Campbell (1990). This was also noted by Farnetani & Richards (1995) who predicted from numerical simulations that the melt produced at a hotspot will contain very low amounts of entrained material. It is possible that we cannot resolve this entrainment process because of the resolution of our PIV measurements. However, even if this is the case, the cross-sectional area of entrained material will be of the same order as the PIV resolution (3.47 mm^2). In contrast, the tracer fields at later times (Figs 4 and 5) indicate that the plume brings a large quantity of material from deep in the fluid ($y \lesssim 50$ mm) to shallower regions. This process can be referred to as 'viscous coupling' or 'viscous entrainment', in which the viscosity of the fluid and the vertical velocity in the hot plume stem causes nearby fluid to be dragged upwards (Hauri *et al.* 1994), in contrast to the 'mechanical entrainment' or 'stirring' of material into the scrolls in the plume head, envisaged by Griffiths & Campbell (1990). Not all of the viscously entrained material is incorporated into the plume head, nor is it guaranteed to undergo any partial melting (Farnetani & Richards 1995) or even pass through the 660 km discontinuity (Kumagai & Kurita 2000; Kumagai *et al.* 2007). However, it indicates that in terms of mixing in the mantle, viscous entrainment plays a far more significant role than mechanical entrainment.

The variation in the rise velocity of material in a plume with depth (Fig. 7) also has implications for the estimation of the rise velocity or upwelling rates of plumes in the mantle from geochemical data (which, as noted above, can also provide the relevant timescales for convection throughout the life cycle of the plume). The rise velocity is typically performed by analysing the Uranium isotopes measured from OIBs, which have a known decay series (White 2010). However, as Hawkesworth & Scherstén (2007) note, although this is sometimes interpreted as representing the rise velocity *throughout* the mantle, it is only representative of the velocity of the material as it passes through the region where decompression melting is occurring.

If we assume that in a hotspot, melt occurs at depths of 0 – 50 km beneath the lithosphere (and the distance between the CMB and the lithosphere to be 2840 km), the corresponding 'melt zone' in the current experiments occurs in the range $y = 249.7$–254.2 mm (indicated by the dashed black line in Fig. 7. The rise velocity of the material in this region is far below the rise velocity of the material

throughout the rest of the fluid domain; i.e. if the Uranium decay series data are used to interpret the rise velocity of the plume in the deep mantle it will significantly underestimate the true value. If the rise time was estimated from the average rise velocity of these signals in the 'melt zone', it would be 3587 min, an overestimation by approximately two orders of magnitude. For the lower Ra experiments, the rise time estimated in the melt zone was also found to be approximately two orders of magnitude smaller than the true value.

This does not indicate that the true ritextcolorblackse times of mantle plumes are two orders of magnitude smaller than the estimates found using the Uranium decay series data, since the dynamics of the magma flow and the effects of phenomena such as phase-transitions have not been taken into account. However, this result demonstrates that analysis of the Uranium series from the melt regions of hotspot does not provide a useful measure of the behaviour of mantle plumes at greater depths.

7 CONCLUSIONS

The dynamics of a thermal plume were examined throughout its life cycle using Lagrangian measurements of the flow field and temperature measurements near the surface. It was found that the life cycle could be divided into four distinct stages based on the surface temperature and the rise velocity of material in the plume stem. The Rising, Steady-Stage and Declining Stages were discussed in terms of the Finite-Time Lyapunov Exponent and tracer fields, with reference to the heating effects of the plume on the region near the fluid surface. The increase in temperature at the surface preceded the arrival of the plume due to the 'thermal halo' surrounding the plume head, and the temperature gradually increased as the head spread out to form a pancake structure at the surface. After the heater was turned off the surface temperature continued to increase for a time before declining exponentially.

The tracer fields suggested negligible amounts of material were mechanically 'stirred' or entrained into the scrolls in the plume head, compared to the amount of material from deep in the fluid domain which rose due to viscous drag from the plume stem. We argued that this is likely to be the dominant process by which plumes contribute to mantle mixing.

The timescales of the plume dynamics found in each experiment were compared and it was shown that all timescales are proportional (or inversely proportional) to the rise time, meaning that it is sufficient to calculated the rise time of mantle in a plume (either in the Rising of Spreading Stages) to know the timescales at all stages of the plume's development. The time lag between the removal of the heat source at the bottom of the fluid and the onset of cooling near the surface was equal to $0.52\tau_r$, and the rate of cooling (which was slightly more uncertain) was found to be $0.27/\tau_r$. A simple analytical model is presented, which shows that under mantle conditions (negligible thermal diffusion) τ_{lag} remains proportional to the rise time regardless of the Rayleigh number, although the ratio of the timescales is closer to unity. These values allow the decline in excess temperature and rates of volcanism in hotspots, such as at Louisville, to be interpreted in terms of a depletion of its source material at the core–mantle boundary.

The plume height and rise velocity of material in the plume were calculated from the tracer fields for various times. The maximum rise velocity was found to occur in the Spreading Stage. The rise velocity was also found to vary significantly with height. This depth-dependence was also discussed in terms of geochemical estimates of the rise velocity based on the decay series of Uranium isotopes, and it was argued that the geochemical predictions are not representative of the rise velocity *throughout* the mantle.

ACKNOWLEDGEMENTS

We would like to thank Stephane Labrosse and two anonymous reviewers for their helpful comments and suggestions. This work was funded by the MAPS Dean's Office at UCL.

REFERENCES

Ballmer, M.D., Ito, G., van Hunen, J. & Tackley, P.J., 2011. Spatial and temporal variability in the Hawaiian hotspot volcanism induced by small-scale convection, *Nat. Geosci.,* **4**(7), 479–382.

Batchelor, G.K., 1954. Heat convection and buoyancy effects in fluids, *Q. J. R. Meteorol. Soc.,* **80,** 339–354.

Bercovici, D. & Mahoney, J., 1994. Double flood basalts and plume head separation at the 660-kilometer discontinuity, *Science,* **266,** 1367–1369.

Cagney, N., Newsome, W.H., Lithgow-Bertelloni, C., Cotel, A., Hart, S.R. & Whitehead, J.A., 2015. Temperature and velocity measurements of a rising thermal plume, *Geochem. Geophys. Geosyst.,* **16,** 1–21.

Campbell, I.H., 2005. Large igneous provinces and the mantle plume hypothesis, *Elements,* **1,** 265–269.

Campbell, I.H. & Griffiths, R.W., 1990. Implications of mantle plume structure for the evolution of flood basalts, *Earth planet. Sci. Lett.,* **99,** 79–93.

Coulliette, D.L & Loper, D.E., 1995. Experimental, numerical and analytical models of mantle starting plumes, *Earth planet. Sci. Lett.,* **92,** 143–167.

Courtillot, V., Davaille, A., Besse, J. & Stock, J., 2003. Three distinct types of hot spots into the Earth's mantle, *Earth planet. Sci. Lett.,* **205,** 295–308.

Davaille, A. & Vatteville, J., 2005. On the transient nature of mantle plumes, *Geophys. Res. Lett.,* **32,** L14309, doi:10.1029/2005GL023029.

Davaille, A., Limare, A., Touitou, F., Kumagai, I. & Vatteville, J., 2011. Anatomy of a laminar starting thermal plume at high Prandtl number, *Exp. Fluids,* **50,** 285–300.

Farnetani, C.G. & Hofmann, A.W., 2010. Dynamics and internal structure of the Hawaiian plume, *Earth planet. Sci. Lett.,* **295,** 231–240.

Farnetani, C.G. & Richards, M.A., 1995. Thermal entrainment and melting in mantle plumes, *Earth planet. Sci. Lett.,* **136,** 251–267.

Farnetani, C.G. & Samuel, H., 2005. Beyond the thermal plume paradigm, *Geophys. Res. Lett.,* **32,** L07311, doi:10.1029/2005GL022360.

Ferziger, J.H., 1998. *Numerical Method for Engineering Applications,* 2nd edn, Wiley-VCH.

French, S.W. & Romanowicz, B., 2015. Broad plumes rooted at the base of the Earth's mantle beneath major hotspots, *Nature,* **525**(7567), 95–99.

Griffiths, R.W., 1986. Thermals in extremely viscous fluids, including the effects of temperature-dependent viscosity, *J. Fluid Mech.,* **166,** 115–138.

Griffiths, R.W. & Campbell, I.H., 1990. Stirring and structure in mantle starting plumes, *Earth planet. Sci. Lett.,* **99,** 66–78.

Griffiths, R.W. & Campbell, I.H., 1991. Interaction of mantle plume heads with the Earth's surface and onset of small-scale convection, *J. geophys. Res.,* **96**(B11), 295–310.

Haller, G., 2015. Lagrangian coherent structures, *Annu. Rev. Fluid Mech.,* **47,** 137–161.

Hart, S.R., Hauri, E.H., Oschmann, L.A. & Whitehead, J.A., 1992. Mantle plumes and entrainment: isotopic evidence, *Science,* **256,** 517–520.

Hauri, E.H., Whitehead, J.A. & Hart, S.R., 1994. Fluid dynamic and geochemical aspects of entrainment in mantle plumes, *J. geophys. Res.,* **99**(B12), 24 275–24 300.

Hawkesworth, C. & Scherstén, A., 2007. Mantle plumes and geochemistry, *Chemical Geology,* **241,** 319–331.

Hofmann, A.W., 1997. Mantle geochemistry: the message from oceanic volcanism, *Nature,* **385**(16), 219–229.

Kaufmann, G. & Lambeck, K., 2009. Mantle dynamics, postglacial rebound and the radial viscosity profile, *Phys. Earth planet. Inter.,* **121,** 301–324.

Kawakatsu, H., Kumar, P., Takei, Y., Shinohara, M., Kanazawa, T., Araki, E. & Suyehiro, K., 2009. Seismic evidence for sharp lithosphere-asthenosphere boundaries of oceanic plates, *Science,* **324,** 499–502.

Kellogg, L.H., 1992. Mixing in the mantle, *Annu. Rev. Earth Planet. Sci.,* **20,** 365–388.

Kellogg, L.H. & King, S.S., 1997. The effect of temperature dependent viscosity on the structure of new plumes in the mantle: results of a finite element model in a spherical, axisymmetric shell, *Earth planet. Sci. Lett.,* **148,** 13–26.

Kerr, R.C. & Mériaux, C., 2004. Structure and dynamics of sheared mantle plumes, *Geochem. Geophys. Geosyst.,* **5**(12), 1–42.

Kumagai, I. & Kurita, K., 2000. On the fate of mantle plumes at density interfaces, *Earth planet. Sci. Lett.,* **179,** 63–71.

Kumagai, I., Davaille, A. & Kurita, K., 2007. On the fate of thermally bouyant mantle plumes at density interfaces, *Earth planet. Sci. Lett.,* **254,** 180–193.

Lay, T., Hernlund, J. & Buffett, B.A., 2008. Core-mantle boundary heat flow, *Nat. Geosci.,* **1,** 25–32.

LeCheminant, A.N. & Heaman, L.M., 1989. Mackenzie igneous events, Canada: Middle Proterozoic hotspot magmatism mackenzie igneous events, Canada: Middle Proterozoic hotspot magmatism associated with ocean opening, *Earth planet. Sci. Lett.,* **96,** 38–48.

Lin, S.-C. & van Keken, P.E., 2006. Dynamics of thermochemical plumes: 1. Plume formation and entrainment of a dense layer, *Geochem. Geophys. Geosyst.,* **7**(2), 1–21.

Lonsdale, P., 1988. Geography and history of the Louisville hotspot chain geography and history of the Louisville hotspot chain in the southwest pacific, *J. geophys. Res.,* **93**(B4), 3078–3104.

Montelli, R., Nolet, G., Dahlen, F.A., Masters, G., Engdahl, E.R. & S.-H., H., 2004. Finite-frequency tomography reveals a variety of plumes in the mantle, *Science,* **303,** 338–343.

Montelli, R., Nolet, G., Dahlen, F.A. & Masters, G., 2006. A catalogue of deep mantle plumes: new results from finite-frequency tomography, *Geochem. Geophys. Geosyst.,* **7**(11), 1–69.

Morgan, W.J., 1971. Convective plumes in the lower mantle, *Nature,* **230,** 42–43.

Moses, E., Zocchi, G. & Libchaber, A., 1993. An experimental study of laminar plumes, *J. Fluid Mech.,* **251,** 581–601.

Nguyen, C.V., Nguyen, T.D., Wells, J.C. & Nakayama, A., 2010. Interfacial PIV to resolve flows in the vicinity of curved surfaces, *Exp. Fluids,* **48,** 577–587.

O'Farrell, C. & Dabiri, J.O., 2010. A Lagrangian approach to identifying vortex pinch-off, *Chaos,* **20,** 017513, doi:10.1063/1.3275499.

Olson, P. & Singer, H., 1985. Creeping plumes, *J. Fluid Mech.,* **158,** 511–531.

Parmentier, E.M. & Turcotte, D.L., 1975. Numerical experiments on the structure of mantle plumes, *J. geophys. Res.,* **80**(32), 4417–4424.

Parnell-Turner, R., White, N., Henstock, T., Murton, B., Maclennan, J. & Jones, S.M., 2014. A continuous 55-million-year record of transient mantle plume activity beneath Iceland, *Nat. Geosci.,* **7,** 914–919.

Raffel, M., Willert, C., Wereley, S. & Kompenhans, J., 2007. *Particle Image Velocimetry,* 2nd edn, Springer.

Ribe, N.M. & Christensen, U.R., 1994. Three-dimensional modeling of plume-lithosphere interaction, *J. geophys. Res.,* **99**(B1), 669–682.

Richards, M.A. & Griffiths, R.W., 1988. Deflection of plumes by mantle shear flow: experimental results and a simple theory, *Geophys. J. Int.,* **95,** 367–376.

Richards, M.A., Duncan, R.A. & Courtillot, V.E., 1989. Flood basalts and hot-spot tracks: plume heads and tails, *Science,* **246**(4926), 103–107.

Schlien, D.J., 1976. Some laminar thermal and plume experiments, *Phys. Fluids,* **19**(8), 1089–1098.

Schubert, G., Turcotte, D.L. & Olson, P., 2001. *Mantle Convection in the Earth and Planets,* vol. 1, 1st edn, Cambridge Univ. Press.

Shadden, S.C., Lekien, F. & Marsden, J.E., 2005. Definition and properties of Lagrangian coherent structures from finite-time Lyapunov exponents in two-dimensional aperiodic flows, *Phys. D,* **212,** 271–304.

van Keken, P.E., Davaille, A. & Vatteville, J., 2013. Dynamics of a laminar plume in a cavity: the influence of boundaries on the steady state stem structure, *Geochem. Geophys. Geosyst.,* **14,** 158–178.

Westerweel, J. & Scarano, F., 2005. Universal outlier detection for PIV data, *Exp. Fluids,* **39,** 1096–1100.

Westerweel, J., Elsinga, G. E. & Adrian, R. J., 2013. Particle image velocimetry for complex and turbulent flows, *Annu. Rev. Fluid Mech.,* **45,** 409–436.

White, W.M., 2010. Oceanic island basalts and mantle plumes: the geochemical perspective, *Annu. Rev. Earth Planet. Sci.,* **38,** 133–160.

Whitehead, J.A. & Luther, D.S., 1975. Dynamics of laboratory diapir and plume models, *J. geophys. Res.,* **80**(5), 705–717.

Whitehead, J.A., Cotel, A., Hart, S., Lithgow-Bertelloni, C. & Newsome, W., 2013. Numerical calculations of two-dimensional large Prandtl number convection in a box, *J. Fluid Mech.,* **729,** 584–602.